BNL-229333-2026-JAAM

Anatomy of Local Structural Disorder of Ni(II) Species in MgCl2-KCl Molten Salts

N. Patra

To be published in "ACS Applied Energy Materials"

February 2026

Nuclear Science & Security Department

Brookhaven National Laboratory

U.S. Department of Energy

USDOE Office of Science (SC), Basic Energy Sciences (BES)

DISCLAIMER

ACS APPLIED ENERGY MATERIALS

www.acsaem.org Article

Anatomy of Local Structural Disorder of Ni(II) Species in $MgCl_2$–KCl Molten Salts

Nirmalendu Patra,* Santanu Roy,* Ellie M. Kim, Vyacheslav S. Bryantsev, Sheng Dai, James F. Wishart, Anatoly I. Frenkel, and Simerjeet K. Gill*

Cite This: https://doi.org/10.1021/acsaem.5c02944 Read Online

ACCESS | Metrics & More | Article Recommendations | Supporting Information

ABSTRACT: Understanding the speciation of metal ions dissolved in molten salts (MS) is critical for enabling a broad range of high-temperature energy applications, including MS nuclear reactors and concentrated solar power plants. However, due to the inherent dynamicity of metal species in the MS environment and the strong temperature dependencies of their multiple coexisting forms, they are difficult to resolve structurally. Herein, we show that combining *in situ* X-ray absorption spectroscopy (XAS) with *ab initio* molecular dynamics (AIMD) simulations is necessary to uncover and quantify the coexisting coordination states of Ni(II) in molten $MgCl_2$–KCl mixtures and explain how the temperature and salt composition control their relative populations. Furthermore, from the interionic angle and distance distributions of nickel in different coordination states obtained from AIMD simulations, it is evident that for each coordination state, the width and skewness of their bonding distributions increase with increasing coordination number. The combination of XAS with first-principles modeling to resolve metastable metal species in MS is critical for understanding their behavior over a wide range of temperatures and chemical environments in nuclear and solar applications.

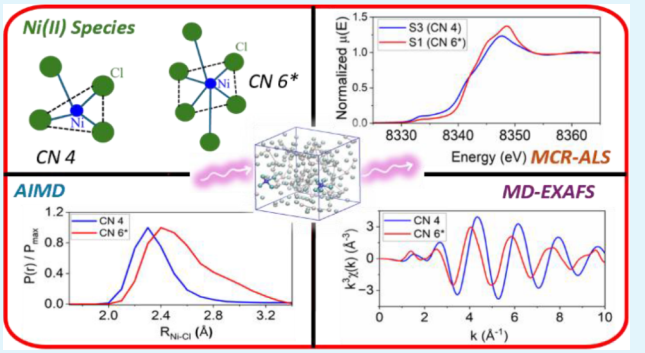

KEYWORDS: *XANES, EXAFS, AIMD, speciation, heterogeneity*

1. INTRODUCTION

Molten salts (MS) are increasingly used in heat transfer systems and thermal energy storage for clean energy applications,[1] which include molten salt reactors (MSRs),[1,2] concentrated solar power plants,[3,4] and high-temperature batteries.[5,6] Compared with conventional light-water reactors, MSRs have safety advantages and higher thermal efficiency. Chloride-based MS are advantageous for fast-spectrum MSRs (which have flexible fuel requirements and can burn actinides) because of their reduced moderating capacity.[7,8] One major challenge in deploying MS for these clean energy technologies is attaining a detailed understanding of their dynamic structural evolution, speciation, and properties as a function of temperature and salt composition. It is imperative to elucidate the underlying solute species–solvent interactions and resulting speciation that directly affect and control the properties of MS.

X-ray absorption spectroscopy (XAS) is a technique that can provide an understanding of solute–solvent interactions and determine quantitative local structures adopted by metal solutes such as divalent nickel (Ni(II)). Nickel is one of the alloying elements of structural materials typically used in MSRs, where it undergoes corrosion. Particularly, XAS provides information about the temperature-dependent coordination numbers (CN), bond distances, and bond distance disorder of metal species and their nearest neighbors. We have employed XAS to investigate the Ni(II) speciation behavior in several chloride-based MS systems.[9−11] We have focused on Ni(II) because it is an important corrosion product and typically exhibits heterogeneous coordination environments in molten chloride salts in the form of multiple coexisting coordination states (CN = 3–6). The commonly used fitting approach for extended X-ray absorption fine structure (EXAFS) is, in general, unable to capture such heterogeneity, resulting in the unlikely outcome of predicting under-coordinated (CN < 3) Ni(II) species.[9,10] $MgCl_2$–KCl is considered a promising salt mixture for MSRs, but the effects of the solvent and temperature on the local structure of Ni(II) speciation are unknown. The complementary technique of optical spectroscopy has been extensively used to study the changes in local coordination geometry of Ni(II) with

Received: September 17, 2025
Revised: November 26, 2025
Accepted: November 28, 2025

composition and temperature in various $MgCl_2$−KCl mixtures.[12,13] These pioneering and meticulous optical studies demonstrated that different Ni(II) coordination state distributions exist as functions of salt composition and temperature, but the models available for interpreting the spectral changes were limited, leading to an underappreciation of the contributions of coordination states with no solid-state analogues, such as the 5-coordinate or highly distorted (low-symmetry) 6-coordinate states.[11]

We have shown in our earlier studies that a multimodal approach combining XAS with *ab initio* molecular dynamics (AIMD) simulations, rate theory, and UV−vis spectroscopy is needed to resolve such complex coordination environments.[9−11,14] AIMD simulations, which provide density functional theory (DFT)-level accuracy of atomic interactions, are computationally expensive and typically limited to short simulation times (picosecond time scales) due to their high computational costs. While at extremely high temperatures AIMD can access different possible coordination states and help generate their ensemble-averaged spectra, the sampling of these states with the correct population is not guaranteed. This can result in a mismatch between the experimental and the computed spectra. In earlier studies,[10] we demonstrated that fine-tuning the populations of different coordination states is possible by using a linear combination fitting (LCF) approach to the EXAFS (LCF-EXAFS) spectra, where we compute EXAFS spectra from AIMD trajectories for different coordination states and vary their mixing fractions until their linear combination is in the best agreement with the experimental spectrum. As a result, the final values of the mixing fractions are obtained and assigned as the correct population of different coordination states.[10] We also showed that rate theory can predict the lifetime of each state and justify the population obtained by LCF-EXAFS. We have explained how, by varying the temperature/solvent composition, these populations can be controlled. Such population analysis has revealed that Ni(II) has mostly 4- and 5-coordinate states, while 3- and 6-coordinate states are much less populated (and, therefore, contribute negligibly to EXAFS) in molten $ZnCl_2$ and KCl−$ZnCl_2$ systems. Interestingly, cobalt (Co(II)), which has only one fewer valence electron than Ni(II), occurs in the 4-coordinate state in molten $ZnCl_2$, demonstrating that our approach can uniquely discern element-specific coordination chemistry and structures.

In our present work, we applied a chemometric approach using principal component analysis (PCA) and multivariate curve resolution-alternating least-squares (MCR-ALS) analysis on X-ray absorption near-edge structure (XANES) spectra to compare the AIMD-EXAFS results with an alternative and model-independent view of the coexisting coordination states of Ni(II) dissolved in molten $MgCl_2$−KCl. Here, we investigate the individual Ni(II) species obtained by the PCA/MCR-ALS analyses of XANES in terms of their variable coordination structures and stability as a function of both the temperature (25−700 °C) and the $MgCl_2$:KCl molar ratio. Specifically, we selected two systems: (1) the global eutectic composition (32 mol % $MgCl_2$, melting point 423 °C[15]), which is most relevant for MSR applications, and (2) the frequently used equimolar off-eutectic composition (50 mol % $MgCl_2$, melting point 487 °C[15]). AIMD simulations are used to calculate free energy profiles, providing insights into the observed speciation and quantifying the probability of finding multiple coordination states and their stabilities at different temperatures and solvent compositions. Some of the most notable insights from the analysis of the AIMD trajectories are the distributions of Cl−Ni−Cl angles and Ni−Cl bond distances for different coordination states, indicating that each coordination state is unique and has distinct skewed bonding distributions. Consequently, the EXAFS signal from each state is distinguishable from that of other states, and therefore, their combined effects dictate the change in the total spectrum as a function of temperature and solvent composition.

2. METHODOLOGY

2.1. X-ray Absorption Spectroscopy Measurements. For XAS, the $MgCl_2$ (anhydrous 99.9%) was purchased from Sigma-Aldrich and further purified via sparging with dry air at 800 °C, fractional distillation at 900 °C, and sparging with Cl_2 gas at 800 °C. The KCl (anhydrous 99.999%, trace metal basis) was purchased from Sigma-Aldrich and further dried under vacuum at 800 °C. The purified $MgCl_2$ and KCl were then fused together under vacuum in a fused silica test tube (10 mm I.D. × 12 mm O.D.) with a #15 Ace-Thred fitting at 32:68 and 50:50 molar ratios by heating to 800 °C until the mixture was molten and visibly homogeneous. 1.0 wt % $NiCl_2$ was then added to the fused $MgCl_2$−KCl mixture and manually mixed under vacuum at 550 °C until the mixture was visibly homogeneous.

The XAS data at the Ni K-edge (8333 eV) were collected at the Inner Shell Spectroscopy (ISS) beamline at the National Synchrotron Light Source II (NSLS-II) at Brookhaven National Laboratory (BNL), New York.[16] The fluorescence data were collected by using a solid-state detector (SSD). The sample temperature was controlled from room temperature to 700 °C using a custom-built furnace. Quartz capillaries (2 mm O.D., 0.01 mm wall thickness) were filled with powder samples under Ar atmosphere and flame-sealed using an H_2 torch. The details of capillary sample preparation for XAS experiments are explained elsewhere.[17] Multiple scans were collected at each temperature for better signal-to-noise ratios. The experimentally obtained raw data (μ (E)) were processed following a standard procedure using the ATHENA program of the Demeter software package.[18] The preprocessing of the data include energy calibration, background subtraction, normalization, and merging of the raw data sets. The merged $\mu(E)$ spectra were extracted to k^2-weighted $\chi(k)$ spectra, then Fourier transformed within the k range 2.5−10.5 $Å^{-1}$ and fitted within the R range 1−2.6 Å using Δk value of 2. The PCA was performed using ATHENA, and the MCR-ALS analysis was performed using the MATLAB-based code MCR-ALS GUI 2.0.[19]

2.2. Ab Initio Molecular Dynamics Simulations. We have previously investigated the structure and dynamics of $MgCl_2$−KCl systems using AIMD simulations.[20,21] A couple of snapshots from these simulations were taken to construct two configurations: (1) a system of 34 $MgCl_2$ + 68 KCl and (2) a system of 52 $MgCl_2$ + 50 KCl. The purpose was to first equilibrate these systems at 550 and 700 °C with a classical force field-based simulation using a polarizable ion mode (PIM)[20,22,23] and then to replace two arbitrarily chosen, well-separated Mg^{2+} ions with two Ni^{2+} ions. This allowed us to create energetically stable configurations of two Ni^{2+} ions in the 32:68 and 50:50 (mol %) mixtures of $MgCl_2$ and KCl for the AIMD simulations. The PIM simulations for 34 $MgCl_2$ + 68 KCl and 52 $MgCl_2$ + 50 KCl mixtures were performed for

https://doi.org/10.1021/acsaem.5c02944
ACS Appl. Energy Mater. XXXX, XXX, XXX−XXX

1.0 ns using CP2K[24] in the isothermal−isobaric ensemble at 1.0 bar and two different temperatures: 550 and 700 °C. The Nosé−Hoover method[25,26] was used to maintain pressure and temperature. The molecular dynamics integration step was set to 1.0 fs. The cutoff for the nonbonded interaction was set to 9 Å. The long-range electrostatics were treated with the Ewald summation method. The densities of the 34 $MgCl_2$ + 68 KCl system converged to their equilibrium values of 1.711 and 1.584 g cm^{-3} at 550 and 700 °C, respectively. For the 52 $MgCl_2$ + 50 KCl system, the converged equilibrated densities are 1.760 and 1.645 g cm^{-3} at 550 and 700 °C, respectively. From these simulations, the structures corresponding to the equilibrium PIM densities were extracted and used as initial configurations (after replacing two Mg^{2+} with two Ni^{2+}) for the AIMD simulations.

All AIMD simulations were performed using the Quickstep module[27] of the CP2K 6.1 package[24] with a time step of 1.0 fs. We employed the Perdew−Burke−Ernzerhof (PBE) exchange-correlation functional[28,29] with Grimme's D3 dispersion correction[30] and the MOLOPT (DZVP) basis set, along with Goedecker−Teter−Hutter pseudopotentials for all ions.[31] A 600 Ry cutoff for the plane wave basis was applied. A Nosé−Hoover chain thermostat with a time constant of 1.0 ps was used for temperature coupling. Trajectories with lengths of at least 130−145 ps were generated for all four systems. We discarded the first 20 ps of each trajectory and used the remaining part for computing the EXAFS spectra and free energy profiles. Spin-unrestricted calculations, considering different initial magnetizations, were performed before the MD steps to ensure that each system was in its electronic ground state with the expected magnetic moment. We employed the orbital transformation method with a FULL_ALL preconditioner and a conjugate gradient minimizer to accelerate self-consistent field (SCF) convergence. For EXAFS calculations, we employed the FEFF9 software[32] and the in-house preprocessing code,[33] following the same protocol discussed in our previous studies.[9] The amplitude reduction factor of S_0^2 = 0.9 was applied to all of the computed EXAFS spectra, which gave the best amplitude correlation between data and MD-EXAFS.

3. RESULTS AND DISCUSSION

3.1. X-ray Absorption Near Edge Structure. We begin the analysis of the local structure of Ni(II) in $MgCl_2$−KCl MS with *in situ* XAS. The Ni K-edge normalized XANES spectra of 1 wt % $NiCl_2$ in the eutectic and equimolar $MgCl_2$−KCl mixtures are shown in Figure 1. The evolution of the XANES spectra with temperature shows noticeable changes in both the pre-edge and mid-edge energy ranges, as well as the white line region. As shown in Figure 1, the XANES spectra show bimodal shapes (an intense peak at 8348 eV and a shoulder at 8345 eV) below the respective melting points for the eutectic (423 °C) and equimolar (487 °C) compositions, which transform to a unimodal shape (only one peak at 8348 eV) upon melting, along with an increase in the pre-edge intensity (insets to Figure 1). These observations agree with our previous studies,[9,11] where Ni(II) hosted in solidified pure $ZnCl_2$ and eutectic LiCl−KCl and $MgCl_2$−NaCl mixtures showed double-peak features in the white line region at room temperature and transitioned to a single peak after melting. The double-peak-like feature can be attributed to distorted octahedral coordination (CN 6*) imposed on the Ni(II) center by the crystalline salt matrix.[9,11] Upon melting of these

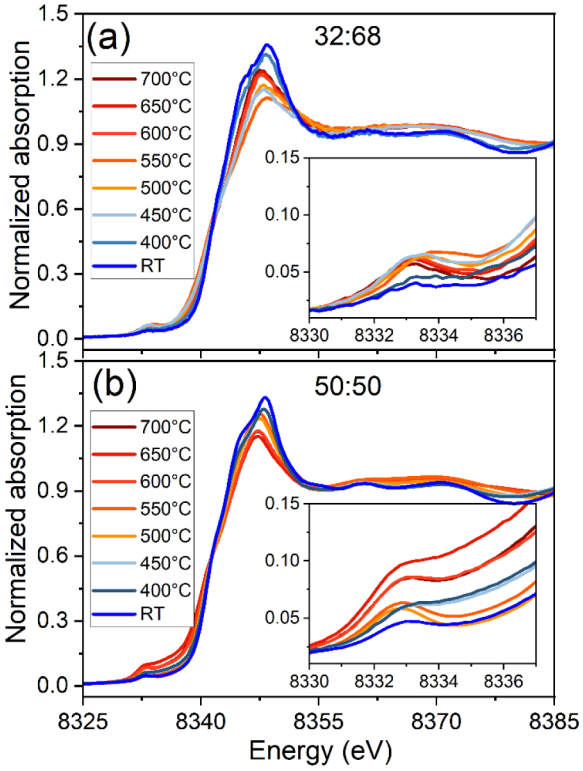

Figure 1. Normalized XANES spectra of Ni(II) in $MgCl_2$−KCl with compositions (a) 32:68 (eutectic) and (b) 50:50 (equimolar). Insets show enlarged views of the pre-edge features. XANES spectra show a change in the pre-edge feature with temperature after melting.

matrices, the CN of Ni(II) decreases. One plausible explanation for the Ni(II) coordination number tending to decrease from RT to temperatures above the melting point is the increased thermal energy in the system, which leads to higher atomic vibrations and disorder in the Ni−Cl bonds. This high thermal vibration weakens the metal−ligand (Ni−Cl) bonds and causes ligands (Cl^-) to dissociate, resulting in a lower coordination number of nickel. Changes in the white line intensity with temperature are very prominent for the eutectic composition from 550 to 600 °C, increasing in intensity instead of decreasing. The spectra remain almost identical in the temperature range between 600 and 700 °C, indicating that the coordination of Ni(II) does not change in this temperature interval. Additionally, the spectra in the post-edge region collected below and above the melting point can be divided into two groups, confirming local Ni(II) structural differences between the solid and molten states. Qualitatively, XANES spectra for the two systems exhibit distinguishable differences in the pre-edge region, such as the eutectic (32:68) mixture showing a more defined and consistent peak intensity with temperature compared to the equimolar (50:50) mixture. This suggests a stronger deviation in coordination symmetry in the equimolar composition than in the eutectic one, indicating a direct influence of salt composition on the local geometry of Ni(II).

To understand the number of distinct Ni coordination states and to deconvolute their mixing fractions in the salt mixtures at different temperatures, we employed PCA analysis in combination with MCR-ALS fitting. While PCA provides a number of unique spectra, MCR-ALS extracts the spectra for each state and their mixing fractions at different temperatures.

https://doi.org/10.1021/acsaem.5c02944
ACS Appl. Energy Mater. XXXX, XXX, XXX−XXX

An energy range of 8320−8400 eV was selected for all spectra in the PCA analysis. The PCA cumulative variance plot, shown in Figure S1 of the Supporting Information, confirms the presence of 3 discernible components in both compositions. Since the variance of the components higher than 3 is small, only 3 components were used to reconstruct the experimental XANES spectra, showing negligible residuals at all temperatures (Figure S2 of the Supporting Information). The experimental spectra at different temperatures were fitted as a linear combination of three component spectra obtained from the MCR-ALS method. The component spectra (S) and their concentrations (C) obtained from MCR-ALS analysis for both $MgCl_2$−KCl compositions are shown in Figure 2. The

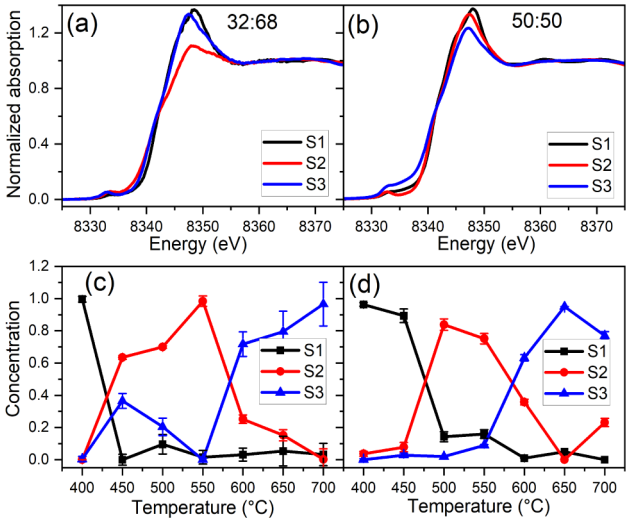

Figure 2. (a, b) The normalized XANES spectra of the MCR-ALS-generated spectra and (c, d) the fraction of mixing of the three species obtained from MCR-ALS in the eutectic and equimolar compositions, respectively, excluding the room-temperature data.

error bars in Figure 2c and d were calculated by performing MCR-ALS analysis on six different postedge energy ranges and represent the average values along with the corresponding statistical deviations from the values shown in Figure 2c and d (Supporting Information Figure S4).

From Figure 2, it is observed that three components (S1, S2, and S3) contribute to the experimental XAS spectra of both systems over the studied temperature range. We observe that S1 is the dominant species for both the salt mixtures at temperatures below the melting point, which includes the measurements at 400 °C for 32:68 and 400 and 450 °C for 50:50. We postulate that S1 represents a distorted octahedral species (CN 6*), as indicated by the broadened white line peak with a small shoulder, as observed in the S1 component XANES spectra (Figure 2a,b) and described above. The species S3, which dominates from 600 to 700 °C, is likely to be a 4-coordinate tetrahedral species, as observed from the AIMD simulations and previously reported UV−vis spectra discussed below. The intermediate species S2 that dominates in the intermediate temperature range (500−550 °C) is most likely to be a 5-coordinate species of Ni(II). In Figure 2c, S2 for 32:68, which maximizes at 550 °C, indicates a stable 5-coordinate species identical to the experimental XANES spectrum collected at 550 °C, as shown in Figure 1a. This similarity indicates a unique characteristic of the Ni(II) species observed at 500 °C, serving as an intermediate coordination state between CN = 4 and 6*. However, the species S3 in the 32:68 composition, which maximizes at high temperature, shows an increase at 450 °C, which is unexpected and can be attributed to anomalous behavior of the system or an outlier from the expected trend due to experimental uncertainty. It is noteworthy that S3 is a major component in both systems after 600 °C, indicating a dominant tetrahedral state at high temperature. Figure S3 of the Supporting Information shows the comparison between the two spectra S1 and S3 of the two systems that represent the coordination before melting and at a temperature above the melting point (≥600 °C), respectively. From this figure, it is observed that while the S1 components derived for the two compositions (which represent the dominant octahedral state prior to melting) are identical to each other, the derived S3 components that represent the dominating tetrahedral state show noticeable differences in the XANES for the two different compositions. This effect of salt composition on the local geometry of Ni(II) species and on the EXAFS spectra is further complemented using AIMD simulations.

3.2. Extended X-ray Absorption Fine Structure. To further substantiate the results obtained from XANES analysis, we turned our attention to the Fourier-transformed EXAFS (FT-EXAFS) data. The phase-uncorrected FT spectra of the two compositions are shown in Figure 3. The first peak appears

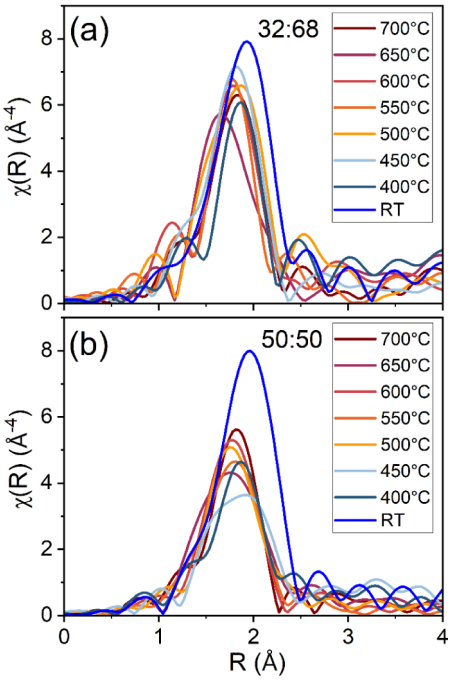

Figure 3. Fourier-transformed k^3-weighted $\chi(k)$ spectra of Ni in (a) eutectic (32:68) and (b) equimolar (50:50) $MgCl_2$−KCl mixtures.

within 1−2.5 Å and corresponds to the Ni−Cl scattering path. Comparing peak positions above the respective melting points, the shift between 450 and 700 °C for the 32:68 composition and between 500 and 700 °C for the 50:50 composition, with respect to their room temperature spectra and below melting points, indicates the overall shortening of the Ni−Cl bond in the molten state. Qualitatively, the shorter bond length in the molten state is correlated with the decrease in CN or change in coordination geometry of Ni as observed in our previous work.[9] The complicated temperature dependence of the FT-

https://doi.org/10.1021/acsaem.5c02944
ACS Appl. Energy Mater. XXXX, XXX, XXX−XXX

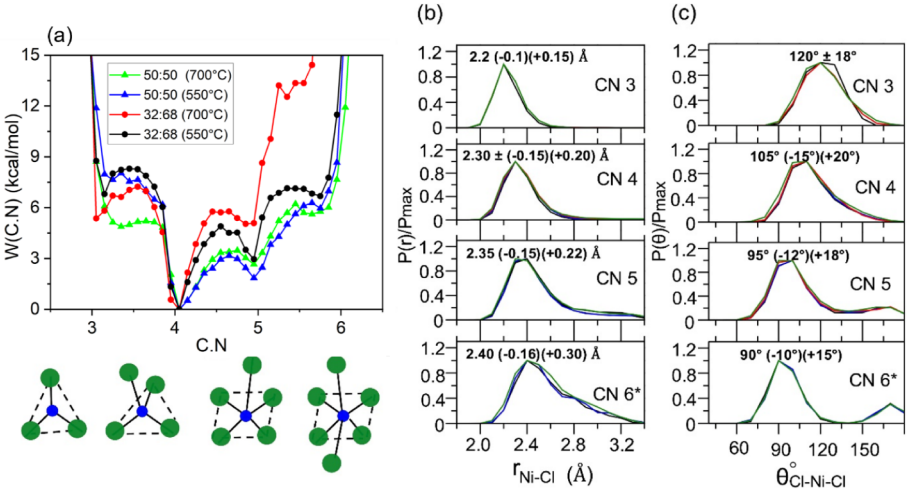

Figure 4. (a) Free energy as a function of chloride coordination number (CN) of Ni(II) for different solvent compositions and temperatures, along with the geometric illustration of different CNs: 3— trigonal, 4—tetrahedral, 5—distorted square pyramidal, and 6*—highly distorted octahedral. (b and c) For the different CN states, the distributions of Ni−Cl bond length (r_{Ni-Cl}) and Cl−Ni−Cl bond angle ($\theta_{Cl-Ni-Cl}$), normalized by the area under the curve, reveal enhanced skewness (or geometric distortion) with increasing CN. The color code is the same as in (a), indicating almost-identical conformational distributions across composition and temperature. The most probable values of r_{Ni-Cl} and $\theta_{Cl-Ni-Cl}$ are mentioned along with their standard deviations. For asymmetric distributions, both left (−) and right (+) deviations are mentioned. Due to poor sampling of CN 6* in 32:68 at 700 °C and CN 3 in 50:50 at 550 °C, the statistics of the corresponding distance and angle distributions are poor, and therefore, they are not included in this plot.

EXAFS spectra highlights a diminished peak at temperatures (400 °C for 32:68 and 450 °C for 50:50) below their respective melting points and then an anomalous increase in the amplitude above the melting points (450 °C for 32:68 and 500 °C for 50:50), followed by a drop in amplitude at higher temperatures. Such anomalous temperature dependence of amplitude suggests the presence of multiple interfering coordination states, resulting in partial cancellation of the oscillation amplitude due to destructive interference of the contributions from these coordination states, as we have observed previously.[9−11] The explanation of the decrease in the amplitude is instead an interplay of the heterogeneously mixed contributions of several coordination states whose mixing fractions and disorder terms change with temperature. The larger drop in the amplitudes of the FT-EXAFS spectra in the molten state of the 50:50 composition compared to 32:68 is indicative of higher overall disorder in the equimolar mixture, given that comparable thermal disorder is expected in both compositions as measured at the same temperatures.

3.3. Ab Initio Molecular Dynamics Simulations. To model how the distribution of Ni−Cl CN[10] varies in the two $MgCl_2$−KCl compositions with temperature, we computed the free energy profiles of CN from AIMD simulations. Figure 4a depicts these free energy profiles, which unequivocally suggest that while the probability of the four-coordinate state (CN 4) is highest (global minimum), the other CN states, such as 3, 5, and 6*, are also sampled in relatively lower populations. By defining the CN 3−6* states, respectively, through the ranges 2.5 < CN < 3.5, 3.5 < CN < 4.5, 4.5 < CN < 5.5, and 5.5 < CN < 6.5, the obtained exact populations from AIMD are listed in Table 1. From these populations, it is clear that for any given composition and temperature, the most populated state is CN 4. For a given composition, a higher temperature (700 °C) enabled sampling of lower CN (CN 3), while the increase in the $MgCl_2$ concentration (50:50 mixture) enabled sampling of higher CNs (CN 5 and CN 6*). The latter can be attributed to the stronger polarizing power of the divalent Mg^{2+}. As the concentration of Mg^{2+} increases, more of the electron density of the Cl^- ions is directed toward the Mg^{2+} ions, making them weaker ligands for Ni^{2+} and reducing repulsion between them, leading to an increase in the populations of CNs greater than four.

Table 1. Populations of Various Ni(II) Coordination States for Different $MgCl_2$−KCl Compositions and Temperatures[a]

$MgCl_2$:KCl	CN	AIMD population (%)	LCF population (%)
32:68 (550 °C)	3	1.4 ± 0.9	0.00
	4	77.3 ± 4.7	67.9 ± 4.1
	5	19.4 ± 2.3	32.1 ± 4.0
	6*	1.9 ± 2.5	0.00
32:68 (700 °C)	3	6.6 ± 1.9	0.00
	4	82.6 ± 5.3	92.2 ± 4.7
	5	10.8 ± 5.3	9.3 ± 5.9
	6*	0.0 ± 0.0	0.00
50:50 (550 °C)	3	0.8 ± 0.8	0.00
	4	66.0 ± 15.2	50.2 ± 5.4
	5	31.3 ± 13.8	49.8 ± 8.1
	6*	1.9 ± 1.8	0.00
50:50 (700 °C)	3	5.2 ± 2.8	0.00
	4	64.1 ± 8.1	86.2 ± 4.7
	5	26.5 ± 7.0	13.8 ± 7.3
	6*	4.2 ± 3.6	0.00

[a]For the MCR-ALS results, the S1 species (Figure 2c and d) correspond to CN 6*, S2 to CN 5, and S3 to CN 4.

To provide a geometric description of the various CNs, we computed probability distributions of the Ni−Cl bond lengths and Cl−Ni−Cl angles of each CN for different mixtures and temperatures and plotted them in Figure 4b,c. Notably, the Ni bond length distribution becomes broader and more skewed with increasing CN, with the deviation from the most-likely value to the half-maximum on the longer bond length side increasing from 0.15 (CN 3) to 0.30 (CN 6*). The most-probable Ni−Cl bond length increases with CN, from 2.2 Å for

https://doi.org/10.1021/acsaem.5c02944
ACS Appl. Energy Mater. XXXX, XXX, XXX−XXX

CN 3 to 2.30 Å for CN 4, 2.35 Å for CN 5, and 2.40 Å for CN 6*, which is consistent with expected results.[11] The angle distribution also exhibits the same trend in skewness, while the most-probable angles shift toward smaller values near the idealized geometries for a given CN. It is noticeable that for CN 3, the distribution peaks at ∼120° and is broad and nearly symmetrical (deviation by ±18°), representing a disordered trigonal geometry. For CN 4, the skewness is enhanced significantly (left deviation 15° and right deviation 20°), representing a largely distorted tetrahedral geometry with a most-probable angle of ∼105°. In going from CN 4 to CN 5, instead of gaining further skewness, the angle distribution splits into a narrower peak with the most-probable angle of ∼95° and a broader peak with the most-probable angle of ∼165°, which suggests the presence of a distribution of distorted square pyramidal geometries. These two peaks get further separated into two well-resolved narrower peaks centered at ∼90° and ∼165° for CN 6*, representing a distorted octahedral geometry when the substantial fraction of long bond lengths (significantly greater than the 2.426 Å observed[34] in octahedral crystalline $NiCl_2$) is taken into account. Overall, the distance and angle distributions for each CN are unique and preserved across different temperatures and compositions. Even for different solvent mixtures, such as $ZnCl_2$−KCl as reported earlier,[10,11] these are preserved as well. That is, even though these geometries are distorted through thermal disorder in the melt, we can treat them as distorted but distinct CN state populations.

Since each CN state is topologically a unique population (with its own CN, mean distance, and mean square relative disorder), it is expected that each state has unique EXAFS spectral features. Specifically, the phase and amplitude should be different for different CNs. In Figure 5, we illustrate this by comparing the k^3-weighted $\chi(k)$ and the FT-EXAFS spectra of different CNs obtained for the 50:50 mixture at 700 °C. It appears that the intensity drops as the CN increases, which may appear surprising as the EXAFS equation[35] suggests that the amplitude should increase with the increasing number of neighbors around the absorber. Nevertheless, the fact that the skewed disorder in the Ni−Cl distance distribution in the first coordination shell progressively increases when going from CN 3 to CN 6* (Figure 4b) is the reason why the behavior in Figure 5b contradicts the expected trend. For CN 6*, the skewness and the associated variance are the largest, suggesting that numerous distinct subensembles of CN 6* exist, each generating EXAFS spectra phase shifted from each other. They partially cancel each other, significantly lowering the intensity of the total EXAFS signal from the CN 6* ensemble compared to that for CN 3. For CN 3, the Ni−Cl distribution is nearly symmetric; distinct CN 3 subensembles that can cause signal cancellations are minimal, leading to the highest amplitude. The behavior of the EXAFS amplitude for CN 4 and CN 5 is also consistent with the trend in the skewness of their Ni−Cl distance distributions. It is also noticeable that the k-space spectrum systematically shifts to the left with increasing CN. This is expected since the most probable Ni−Cl distance increases due to the CN increase as shown in Figure 4a, which is further reflected in the systematic right shifts in the R-space spectrum.

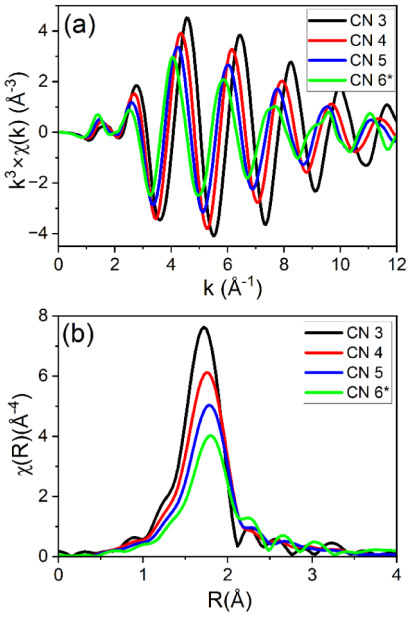

Figure 5. From AIMD simulations, (a) the computed k^3-weighted $\chi(k)$ and (b) FT-EXAFS spectra of the 50:50 composition showing the phase and amplitude shifts between different coordination states. In k-space, the oscillation shifts to the left (smaller k), and consequently, the peak in FT-EXAFS shifts to the right (larger R) with increasing CN. The amplitude in both cases dropped with the increase in CN.

From the knowledge of the geometry of a CN state across temperatures or compositions, it is interesting to find out how the EXAFS spectrum of a specific CN state changes with the change in temperature or composition. To address this, we have compared the EXAFS spectra for CN 4 in Figure 6 for each pair of compositions and temperatures. It turns out that the effects are rather small and can be correlated to the corresponding changes in the surrounding structural ordering. Since the solvent is composed of $MgCl_2$ and KCl, its structural ordering is predominantly dictated by the Mg^{2+} ion. These divalent ions form networks via Cl^- sharing[20,21] and the Ni^{2+} ions join the network via Cl^- sharing. Changing the temperature or the $MgCl_2$:KCl composition alters the network of Cl^--bridged Mg^{2+} ions and the Cl^--shared Ni^{2+}−Mg^{2+} interactions. To illustrate this, in Figure 7, we show the 2D-free energy as functions of the Ni−Mg distance and the number of Cl^- ions shared between these cations (Figure 7a) and the number of other Mg^{2+} ions simultaneously coordinating with the Ni^{2+}−Mg^{2+} pair mediated by Cl^- ions (Figure 7b) (see ref 10 for mathematical definition). At lower temperature and higher Mg^{2+} concentration (i.e., 550 °C, 50 mol %), where Mg^{2+} ions form more extensive networks, a Ni^{2+} ion coordinates with 2 or 1 Mg^{2+} ions (i.e., 1 or 0 Mg^{2+} shared between the Ni−Mg pair, see Figure 7b) through sharing 2 or 1 Cl^- ions (and occasionally 3 Cl^- ions for the 50:50 composition, see Figure 7a). At higher temperature and lower Mg^{2+} concentration (i.e., 700 °C, 32 mol %), where Mg^{2+} ions form smaller networks due to lower concentration and enhanced thermal disorder, a Ni^{2+} ion coordinates with only 1 Mg^{2+} ion (i.e., 0 Mg^{2+} shared between the Ni−Mg pair, see Figure 7b) through predominantly sharing 2 or 1 Cl^- (Figure 7a). Both temperature-induced structural disorder and the change in the composition via an increase in the Mg^{2+} concentration led to a small drop in the EXAFS amplitude. The increase in the Mg^{2+} concentration weakens the Ni−Cl interaction strength via polarization induced by Mg^{2+}, causing a diminished EXAFS signal.

https://doi.org/10.1021/acsaem.5c02944
ACS Appl. Energy Mater. XXXX, XXX, XXX−XXX

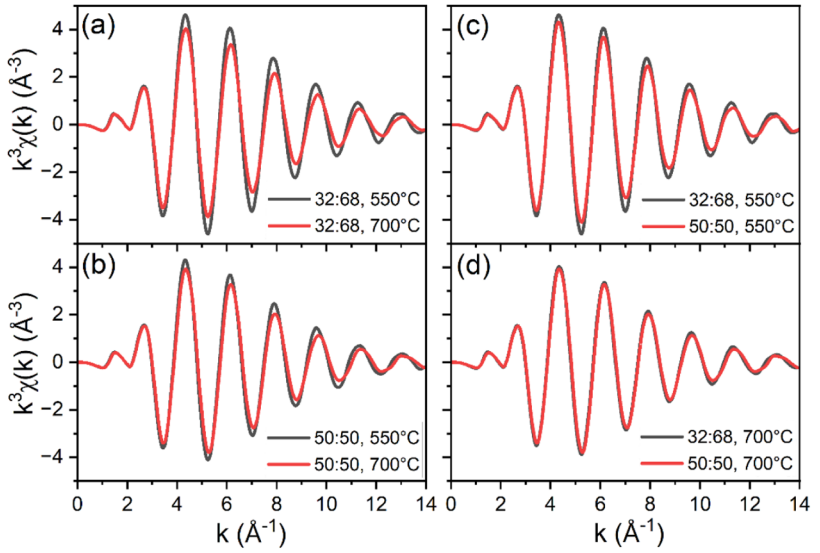

Figure 6. (a, b) show the temperature dependence of the EXAFS spectra for CN 4 species at a given salt composition, and (c, d) show the compositional dependence of the EXAFS spectra for CN 4 species at a given temperature.

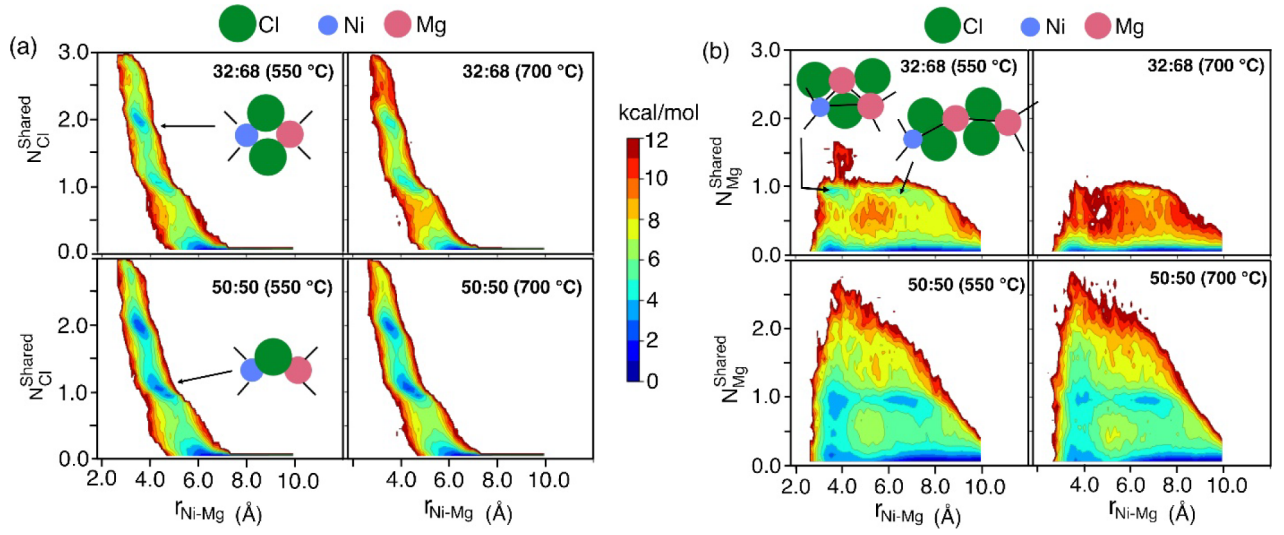

Figure 7. 2D-free energy surfaces highlighting the number of Cl^- ions (a) and the number of Mg^{2+} ions (b) shared between (or coordinated jointly to) a Ni^{2+} ion and a Mg^{2+} ion separated by distance, r_{Ni-Mg}, revealing the effects of temperature and solvent composition changes. The cartoons specifically point to the states of 2 or 1 Cl^- sharing (a) and 1 Mg^{2+} sharing between the Ni−Mg pair mediated by Cl^-.

As discussed above, the presence of multiple CNs of metal solutes, such as nickel, in molten salts can lead to destructive interference of their phase- and amplitude-shifted EXAFS spectra.[9,10] Since the variation in the composition and temperature only slightly affects the EXAFS spectrum for a given CN state, the relative populations of all the CN states determine the total EXAFS spectrum. In Table 1, we list the populations of different CN states sampled in AIMD and depict the total spectra obtained by the MD-population-weighted sum of their EXAFS spectra in Figure 8. It should be noted that AIMD does not guarantee adequate sampling of the populations of these states due to the limitations of the simulation length and DFT accuracy. Therefore, it is expected that the total MD-population-weighted spectra, namely MD-EXAFS may fail to reproduce the experimental spectra. We previously introduced an approach to correct the population of different states via the linear combination fitting of the computed spectra of these states to an experimental spectrum. Within this LCF-EXAFS approach, as the populations get adjusted, an excellent agreement between the computed and experimental spectra can be achieved.[10] We note here that while the LCF-EXAFS is presented in *R*-space in Figure 8, the fitting was done in *k*-space through the range of 2.9−10.0 Å^{-1} and by setting the absorption energy of each experimental spectrum to the same value (8340 eV). The energy shift value was determined by aligning the reference channels to the first derivative of a Ni foil standard. The LCF-corrected populations are also listed in Table 1.

For all compositions and temperatures, we find excellent agreement between the LCF-EXAFS and experimental data. The population obtained from MCR-ALS (Figure 2c and d) also agrees with LCF-EXAFS at 700 °C. MD-EXAFS is in excellent agreement with the experimental spectrum for the 50:50 mixture at 700 °C, while for other cases, MD-EXAFS shows a slight amplitude overestimation with respect to the experimental observation, pointing to the sampling issue at the

https://doi.org/10.1021/acsaem.5c02944
ACS Appl. Energy Mater. XXXX, XXX, XXX−XXX

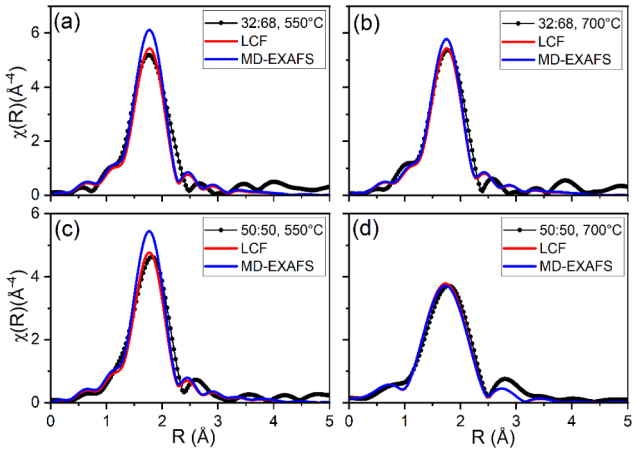

Figure 8. Radial distributions derived from nickel EXAFS spectra from experiment, linear combination fitting (LCF), and MD-EXAFS for Ni(II) in $MgCl_2$−KCl with molar ratios (a)−(b) 32:68 at 550 and 700 °C and (c)−(d) 50:50 at 550 and 700 °C, highlighting excellent agreement between LCF-EXAFS and experimental spectra.

lower temperature or DFT inaccuracy. From Table 1, we find that LCF-EXAFS cannot recognize CN 3 and CN 6*, which is justified since they are rarely sampled in AIMD (populations <7 mol %, considering all cases). While the exact populations of CN 4 and CN 5 from AIMD and LCF are quantitatively different, both approaches exhibit the same trend in the population change as a function of composition/temperature change. For instance, for a given composition, increasing the temperature reduces the population of CN 5 and increases the population of CN 4. For a given temperature, increasing the Mg^{2+} composition causes the opposite behavior; i.e., the population of CN 5 increases and the population of CN 4 decreases. Overall, MD-EXAFS and LCF-EXAFS qualitatively portray the same picture of Ni-speciation in the $MgCl_2$−KCl mixture. The populations of various coordination structures adopted by Ni obtained from MCR-ALS (considering the equivalency of the species S1 to CN 6*, S2 to CN 5, and S3 to CN 4) agree very well with the population of these species obtained from LCF, as shown in Table 1, at 700 °C. Such agreement between the end-state populations obtained by both approaches at high temperature serves as a cross-validation of these methods and strengthens the reliability of both approaches at high temperature (700 °C). It should be noted that the MCR-ALS population deviates from LCF at 550 °C due to the discrepancies in the experimental data described in the MCR-ALS section.

3.4. UV−vis Spectroscopy of Ni(II) in the Salt Mixtures. Though primarily our focus in this study is to connect XAS and AIMD to resolve the heterogeneity of coordination states and their structural ordering adopted by Ni(II) in $MgCl_2$−KCl MS at different temperatures and compositions, we obtain complementary insights by referring to the optical absorption spectra of Ni(II) in molten $MgCl_2$−KCl mixtures that were reported by Brynestad and Smith.[12] We focus on the spectra they reported for $KMgCl_3$, which is the equimolar (50:50) $MgCl_2$−KCl system and K_2MgCl_4, where the $MgCl_2$−KCl ratio is 33:67, very close to the eutectic composition (32:68) investigated above.

For this purpose, we digitized the optical spectra in Figures 1a and 2a from Brynestad and Smith's work,[12] as shown in parts (a) and (b) of Supporting Information Figure S5, and interpreted the spectra based on analyses articulated in our recent publication[11] and review article.[14] The difference between Brynestad and Smith's interpretation of their measured spectra and our interpretation is that they concluded the two species in equilibrium contributing to the observed spectra are a 4-coordinate "T" center and a 6-coordinate "O" center, short for tetrahedral and octahedral, respectively. As elaborated above, our analysis, which is informed by XAS and AIMD simulations, includes CNs 3, 4, 5, and 6*, with CNs 4 and 5 making the dominant contributions to the population profile. In our recent paper,[11] we articulated reasons for associating the absorption signatures of different coordination states with their characteristic wavenumber regions of the optical spectrum, which are depicted with colored bars in Figure S5 of the Supporting Information. The characteristic absorption region for the distorted 6-coordinate species (CN 6*) is indicated by a blue band between 19 000 and 21 000 cm^{-1}, that for the 5-coordinate species (CN 5) is indicated by a green band between 17 000 and 19 000 cm^{-1}, and that for the 4-coordinate species (CN 4) is indicated by a red band between 13 000 and 17 000 cm^{-1}. (The borders of these regions are approximate and effectively overlap to some extent.)

Comparing the measured temperature-dependent spectra of near-eutectic 33:67 $MgCl_2$−KCl in Figure S5a with the band assignments for CN 4 and CN 5, we see that they are generally consistent with the populations in Table 1 obtained from AIMD simulations and LCF-EXAFS analysis of the eutectic mixture, and the dominant contribution is from CN 4, with some contribution from CN 5. In the equimolar mixture (Figure S5b), in addition to the absorption from CN 4, there is a more significant contribution from CN 5, which decreases in favor of CN 4 with increasing temperature. This is consistent with the higher fraction of Mg^{2+} ions, making the equimolar mixture less chlorobasic than the eutectic one. For the lower-temperature 483 and 526 °C spectra, there is a suggestion of a spectral contribution at 20 000 cm^{-1} from the CN 6* coordination state, which is consistent with the MCR-ALS analysis of the XANES data. To extend the comparison further, we include the spectra of Ni(II) in eutectic (44:56) $MgCl_2$−NaCl that we reported in our earlier work[11] in Figure S5c. Having higher charge density, the sodium cation polarizes chloride anions more than the potassium cation does. The result is that even with 6 mol % fewer Mg^{2+} ions compared to equimolar $MgCl_2$−KCl, the eutectic (44:56) $MgCl_2$−NaCl mixture is less chlorobasic, and the average CN of Ni(II) is higher than in equimolar $MgCl_2$−KCl. At lower temperatures (500 and 550 °C), the contribution from the population of CN 6* in eutectic $MgCl_2$−NaCl is more prominent, in addition to the larger contribution from CN 5. As the CNs decrease with increasing temperature, the spectra and CN distributions of Ni(II) in eutectic $MgCl_2$−NaCl and equimolar $MgCl_2$−KCl begin to look very similar.

4. CONCLUSION

We combined XAS and AIMD simulations with free energy analysis to analyze the speciation of Ni(II) in eutectic and equimolar molten $MgCl_2$−KCl mixtures. Utilizing this approach, we successfully resolved the structural heterogeneity of Ni(II) coordination in these environments. Specifically, the relative stabilities of a set of coexisting multiple coordination states at different temperatures and solvent compositions were determined. XANES analysis shows a clear transition from

https://doi.org/10.1021/acsaem.5c02944
ACS Appl. Energy Mater. XXXX, XXX, XXX−XXX

higher-coordinated species to lower-coordinated species with increasing temperature. Deconvolution of XANES data sets using PCA and MCR-ALS shows the presence of three major Ni(II) species in the $MgCl_2$−KCl mixtures that appear in different temperature regions. Complementing this finding, EXAFS spectroscopy, AIMD-based modeling (particularly LCF-EXAFS modeling), and free energy profiles helped us determine the populations of the different coexisting coordination states of Ni(II), suggesting that distorted tetrahedral 4-coordinate and distorted square pyramidal 5-coordinate species are the dominant coordination states. The 4-coordinate state is the most stable in the high-temperature range (550 to 700 °C) for both compositions. The five-coordinate species have a larger population fraction in the 50:50 equimolar composition as compared to the 32:68 eutectic composition. The higher Mg^{2+} content in the equimolar composition results in stronger polarization of the Cl^- ions, making them weaker ligands for Ni(II) and thereby increasing the average Ni CN. The Ni−Cl bond length and Cl−Ni−Cl angle distribution analysis revealed that characteristic Ni(II) coordination geometries remain remarkably consistent among different salt compositions, even as the relative populations of the coordination states vary significantly with composition and temperature. Skewness of the bond length and angle distributions increases significantly with an increase in CN, consistent with the weakening of specific Ni−Cl interactions as the CN increases. Our approach of combining XAS and AIMD enables a better understanding of the complexity of Ni(II) coordination structures and lays the foundation for studying the speciation of other important corrosion and fission products in MS.

■ ASSOCIATED CONTENT

Data Availability Statement

The digital data for all figures, tables, charts, and any other media contained in this publication and its associated ESI files will be made accessible in the Molten Salts in Extreme Environments (MSEE) Community of the Zenodo repository under Digital Object Identifier (DOI): https://doi.org/10.5281/zenodo.17860555.

Supporting Information

The Supporting Information is available free of charge at https://pubs.acs.org/doi/10.1021/acsaem.5c02944.

Principal component analysis on XANES data, MCR-ALS method, digitized UV−vis absorbance data (PDF)

■ AUTHOR INFORMATION

Corresponding Authors

Nirmalendu Patra − *Nuclear Science and Technology Department, Brookhaven National Laboratory, Upton, New York 11973, United States;* orcid.org/0000-0002-6632-5882; Email: npatra1@bnl.gov

Simerjeet K. Gill − *Nuclear Science and Technology Department, Brookhaven National Laboratory, Upton, New York 11973, United States;* orcid.org/0000-0003-4955-4509; Email: gills@bnl.gov

Santanu Roy − *Chemical Sciences Division, Oak Ridge National Laboratory, Oak Ridge, Tennessee 37831, United States;* orcid.org/0000-0001-6991-8205; Email: roys@ornl.gov

Authors

Ellie M. Kim − *Department of Chemistry, University of Tennessee, Knoxville, Tennessee 37916, United States;* orcid.org/0000-0003-4906-1261

Vyacheslav S. Bryantsev − *Chemical Sciences Division, Oak Ridge National Laboratory, Oak Ridge, Tennessee 37831, United States;* orcid.org/0000-0002-6501-6594

Sheng Dai − *Chemical Sciences Division, Oak Ridge National Laboratory, Oak Ridge, Tennessee 37831, United States; Department of Chemistry, University of Tennessee, Knoxville, Tennessee 37916, United States;* orcid.org/0000-0002-8046-3931

James F. Wishart − *Chemistry Division, Brookhaven National Laboratory, Upton, New York 11973, United States;* orcid.org/0000-0002-0488-7636

Anatoly I. Frenkel − *Chemistry Division, Brookhaven National Laboratory, Upton, New York 11973, United States; Department of Materials Science and Chemical Engineering, Stony Brook University, Stony Brook, New York 11794, United States;* orcid.org/0000-0002-5451-1207

Complete contact information is available at: https://pubs.acs.org/10.1021/acsaem.5c02944

Author Contributions

N.P. and S.K.G. conceived the idea and designed the experiment. E.M.K. and S.D. are responsible for salt synthesis. N.P. performed the synchrotron XAS experiment and analyzed the data. V.S.B. and S.R. performed the AIMD simulations. S.R. performed the FEFF calculation. N.P. performed the LCF on AIMD simulations, and N.P. and S.R. drafted the manuscript. J.F.W., A.I.F., and S.K.G. supervised the project. All authors participated in reviewing and editing the manuscript. All authors have given approval to the final version of the manuscript.

Notes

The authors declare no competing financial interest.

■ ACKNOWLEDGMENTS

This work was supported as part of the Molten Salts in Extreme Environments Energy Frontier Research Center, funded by the U.S. Department of Energy (DOE), Office of Science. Brookhaven National Laboratory (BNL) and Oak Ridge National Laboratory (ORNL) are operated under DOE Contract Nos. DE-SC0012704 and DE-AC05-00OR22725, respectively. Work at the University of Tennessee was performed under subcontract to BNL. This research used resources of the ISS (8-ID) beamline at the NSLS-II, operated by BNL under Contract No. DE-SC0012704, a DOE Office of Science User Facility. The authors thank Dr. Akhil Tayal for helping with the XAS data collection at the ISS beamline. The authors thank Dr. Ruchi Gakhar and Dr. Alejandro Ramos-Ballesteros for valuable discussions on the UV−vis data. This research used resources of the Compute and Data Environment for Science (CADES) at the ORNL and the National Energy Research Scientific Computing Center (NERSC), which are supported by the Office of Science of the DOE under Contract Nos. DE-AC05-00OR22725 and DE-AC02-05CH11231, respectively.

REFERENCES

(1) Roper, R.; Harkema, M.; Sabharwall, P.; Riddle, C.; Chisholm, B.; Day, B.; Marotta, P. Molten salt for advanced energy applications: A review. *Ann. Nucl. Energy* **2022**, *169*, 108924−108942.

(2) Serp, J.; Allibert, M.; Beneš, O.; Delpech, S.; Feynberg, O.; Ghetta, V.; Heuer, D.; Holcomb, D.; Ignatiev, V.; Kloosterman, J. L.; Luzzi, L.; Merle-Lucotte, E.; Uhlir, J.; Yoshioka, R.; Zhimin. D.The molten salt reactor (MSR) in Generation IV: Overview and perspectives. *Prog. Nucl. Energy* **2014**, *77*, 308−319.

(3) Bonk, A.; Sau, S.; Uranga, N.; Hernaiz, M.; Bauer, T. Advanced heat transfer fluids for direct molten salt line-focusing CSP plants. *Prog. Energy Combust. Sci.* **2018**, *67*, 69−87.

(4) Ding, W.; Shi, H.; Jianu, A.; Xiu, Y.; Bonk, A.; Weisenburger, A.; Bauer, T. Molten chloride salts for next generation concentrated solar power plants: Mitigation strategies against corrosion of structural materials. *Solar Energy Mater. Solar Cells* **2019**, *193*, 298−313.

(5) Boretti, A.; Castelletto, S. High-temperature molten-salt thermal energy storage and advanced-Ultra-supercritical power cycles. *J. Energy Storage* **2021**, *42*, 103143−103156.

(6) Dong, Q.; Tian, Q.; Zhang, S.; Zhang, W.; Chen, Z.; Han, X.; Hu, W. Novel zinc-based molten salt batteries with high voltages in medium temperature environment. *J. Power Sources* **2022**, *550*, 232143−232153.

(7) Dumaire, T.; Ocádiz-Flores, J. A.; Konings, R. J. M.; Smith, A. L. A promising fuel for fast neutron spectrum Molten Salt Reactor: NaCl-ThCl4-PuCl3. *Calphad* **2022**, *79*, 102496−102505.

(8) Yin, H.; Lin, J.; Hu, B.; Liu, W.; Guo, X.; Liu, Q.; Tang, Z. Thermodynamic description of the constitutive binaries of the NaCl-KCl-UCl3-PuCl3 system. *Calphad* **2020**, *70*, 101783−101792.

(9) Gill, S. K.; Huang, J.; Mausz, J.; Gakhar, R.; Roy, S.; Vila, F.; Topsakal, M.; Phillips, W. C.; Layne, B.; Mahurin, S.; Halstenberg, P.; Dai, S.; Wishart, J. F.; Bryantsev, V. S.; Frenkel, A. I. Connections between the Speciation and Solubility of Ni(II) and Co(II) in Molten ZnCl2. *J. Phys. Chem. B* **2020**, *124* (7), 1253−1258.

(10) Roy, S.; Liu, Y.; Topsakal, M.; Dias, E.; Gakhar, R.; Phillips, W.; Wishart, J.; Leshchev, D.; Halstenberg, P.; Dai, S.; Gill, S. K.; Frenkel, A. I.; Bryantsev, V. S.A Holistic Approach for Elucidating Local Structure, Dynamics, and Speciation in Molten Salts with High Structural Disorder. *J. Am. Chem. Soc.* **2021**, *143* (37), 15298−15308.

(11) Liu, Y.; Topsakal, M.; Zheng, K.; Betancourt, L. E.; Woods, M.; Roy, S.; Patra, N.; Leshchev, D.; Halstenberg, P.; Maltsev, D. S.; Dai, S.; Ivanov, A. S.; Bryantsev, V. S.; Wishart, J. F.; Gakhar, R.; Frenkel, A. I.; Gill, S. K. Correlative analysis of Ni(ii) coordination states in molten salts using a combination of X-ray and optical spectroscopies and simulations. *Chem. Sci.* **2025**, *16* (23), 10414−10423.

(12) Brynestad, J.; Smith, G. P. Electronic Spectra and Coordination Geometry of Nickel Centers in Liquid Mixtures of Magnesium Chloride and Potassium Chloride. *J. Chem. Phys.* **1967**, *47* (9), 3190−3193.

(13) Brynestad, J.; Yakel, H. L.; Smith, G. P. Temperature Dependence of the Absorption Spectrum of Nickel(II)-Doped KMgCl3 and the Crystal Structure of KMgCl3. *J. Chem. Phys.* **1966**, *45* (12), 4652−4664.

(14) Zheng, K.; Patra, N.; Marcella, N.; Ivanov, A. S.; Wishart, J. F.; Ballesteros, A. R.; Gakhar, R.; Dai, S.; Roy, S.; Bryantsev, V. S.; et al. X-Ray Absorption Studies of Local Structure of Dilute Ionic Species in Molten Salts. *Chem. Methods* **2025**, *5* (7), No. e202400097.

(15) Villada, C.; Ding, W.; Bonk, A.; Bauer, T. Simulation-Assisted Determination of the Minimum Melting Temperature Composition of MgCl2−KCl−NaCl Salt Mixture for Next-Generation Molten Salt Thermal Energy Storage. *Front. Energy Res.* **2022**, *10*, 809663.

(16) Leshchev, D.; Rakitin, M.; Luvizotto, B.; Kadyrov, R.; Ravel, B.; Attenkofer, K.; Stavitski, E. The Inner Shell Spectroscopy beamline at NSLS-II: a facility for in situ and operando X-ray absorption spectroscopy for materials research. *J. Synchrotron Radiat.* **2022**, *29* (4), 1095−1106.

(17) Patra, N.; Ballesteros, A. R.; Iwamatsu, K.; Leshchev, D.; Bawane, K. K.; Gakhar, R.; LaVerne, J. A.; Frenkel, A. I.; Wishart, J. F.; Gill, S. K. Electron Radiation-Induced Nickel Nanoparticle Formation in KCl-ZnCl2 Eutectic Molten Salt Using X-ray Absorption Spectroscopy. *J. Phys. Chem. C* **2024**, *128* (22), 9105−9115.

(18) Ravel, B.; Newville, M. ATHENA, ARTEMIS, HEPHAESTUS: data analysis for X-ray absorption spectroscopy using IFEFFIT. *J Synchrotron Rad.* **2005**, *12* (4), 537−541.

(19) Camp, C. H., Jr pyMCR: A Python Library for Multivariate Curve Resolution Analysis with Alternating Regression (MCR-AR). *J. Res. Natl. Inst. Stand. Technol.* **2019**, *124*, 1−10.

(20) Wu, F.; Roy, S.; Ivanov, A. S.; Gill, S. K.; Topsakal, M.; Dooryhee, E.; Abeykoon, M.; Kwon, G.; Gallington, L. C.; Halstenberg, P.; Layne, B.; Ishii, Y.; Mahurin, S. M.; Dai, S.; Bryantsev, V. S.; Margulis, C. J. Elucidating Ionic Correlations Beyond Simple Charge Alternation in Molten MgCl2−KCl Mixtures. *J. Phys. Chem. Lett.* **2019**, *10* (24), 7603−7610.

(21) Roy, S.; Brehm, M.; Sharma, S.; Wu, F.; Maltsev, D. S.; Halstenberg, P.; Gallington, L. C.; Mahurin, S. M.; Dai, S.; Ivanov, A. S.; Margulis, C. J.; Bryantsev, V. S. Unraveling Local Structure of Molten Salts via X-ray Scattering, Raman Spectroscopy, and Ab Initio Molecular Dynamics. *J. Phys. Chem. B* **2021**, *125* (22), 5971−5982.

(22) Ohtori, N.; Salanne, M.; Madden, P. A. Calculations of the thermal conductivities of ionic materials by simulation with polarizable interaction potentials. *J. Chem. Phys.* **2009**, *130* (10), 104507.

(23) Ishii, Y.; Kasai, S.; Salanne, M.; Ohtori, N. Transport coefficients and the Stokes−Einstein relation in molten alkali halides with polarisable ion model. *Mol. Phys.* **2015**, *113* (17−18), 2442−2450.

(24) Hutter, J.; Iannuzzi, M.; Schiffmann, F.; VandeVondele, J. cp2k: atomistic simulations of condensed matter systems. *WIREs Comput. Mol. Sci.* **2014**, *4*, 15−25.

(25) Nosé, S. A unified formulation of the constant temperature molecular dynamics methods. *J. Chem. Phys.* **1984**, *81* (1), 511−519.

(26) Hoover, W. G. Canonical dynamics: Equilibrium phase-space distributions. *Phys. Rev. A* **1985**, *31* (3), 1695−169.

(27) VandeVondele, J.; Krack, M.; Mohamed, F.; Parrinello, M.; Chassaing, T.; Hutter, J. Quickstep: Fast and accurate density functional calculations using a mixed Gaussian and plane waves approach. *Comput. Phys. Commun.* **2005**, *167* (2), 103−128.

(28) Perdew, J. P.; Burke, K.; Ernzerhof, M. Perdew, Burke, and Ernzerhof Reply. *Phys. Rev. Lett.* **1998**, *80* (4), 891−891.

(29) Perdew, J. P.; Burke, K.; Ernzerhof, M. Generalized Gradient Approximation Made Simple. *Phys. Rev. Lett.* **1996**, *77* (18), 3865−3868.

(30) Grimme, S.; Antony, J.; Ehrlich, S.; Krieg, H. A consistent and accurate ab initio parametrization of density functional dispersion correction (DFT-D) for the 94 elements H-Pu. *J. Chem. Phys.* **2010**, *132* (15), 154104.

(31) Goedecker, S.; Teter, M.; Hutter, J. Separable dual-space Gaussian pseudopotentials. *Phys. Rev. B* **1996**, *54* (3), 1703−1710.

(32) Rehr, J. J.; Kas, J. J.; Vila, F. D.; Prange, M. P.; Jorissen, K. Parameter-free calculations of X-ray spectra with FEFF9. *Phys. Chem. Chem. Phys.* **2010**, *12* (21), 5503−5513.

(33) Roy, S. *"66santanu/FEFF-Input-MD-EXAFS: Create_FEFF_Input*; Zenodo, 2023. https://doi.org/10.5281/zenodo.10045182.

(34) Ferrari, A.; Braibanti, A.; Bigliardi, G. Refinement of the crystal structure of NiCl2 and of unit-cell parameters of some anhydrous chlorides of divalent metals. *Acta Crystallogr.* **1963**, *16*, 846−847.

(35) Schenter, G. K.; Fulton, J. L. Molecular Dynamics Simulations and XAFS (MD-XAFS). In. *XAFS Techniques for Catalysts, Nanomaterials, and Surfaces*. Iwasawa, Y.; Asakura, K.; Tada, M., Eds.; Springer, pp. 251−270, 2017

https://doi.org/10.1021/acsaem.5c02944
ACS Appl. Energy Mater. XXXX, XXX, XXX−XXX